Solid State Communications 183 (2014) 22–26

Contents lists available at ScienceDirect

Solid State Communications

journal homepage: www.elsevier.com/locate/ssc

Local structure relaxation in nanosized tungstates

A. Anspoks [a], A. Kalinko [a,b], J. Timoshenko [a], A. Kuzmin [a,*]

[a] Institute of Solid State Physics, University of Latvia, Kengaraga street 8, LV-1063 Riga, Latvia
[b] Synchrotron SOLEIL, l'Orme des Merisiers, Saint-Aubin, BP 48, 91192 Gif-sur-Yvette, France

ARTICLE INFO

Article history:
Received 11 September 2013
Received in revised form
23 December 2013
Accepted 24 December 2013
by F. Peeters
Available online 2 January 2014

Keywords:
A. Nanostructures
C. EXAFS
E. Inelastic light scattering
E. Synchrotron radiation

ABSTRACT

The atomic structure of nanosized and microcrystalline tungstates $MeWO_4$ (Me=Co, Ni, Cu, Zn), synthesized by co-precipitation technique, has been studied by x-ray absorption spectroscopy at the W L_3-edge and Co/Ni/Cu/Zn K-edges, x-ray diffraction, Raman and Fourier transform infrared spectroscopies. The distortion of metal–oxygen octahedra is caused by the electron–lattice coupling and is further enhanced in nanosized tungstates due to formation of the double tungsten–oxygen bonds at the nanoparticle surface.

1. Introduction

The atomic structure of nanocrystalline materials differs from that in the bulk due to relaxation phenomena [1]. The unit-cell volume compression is common for metal nanoparticles [2,3], whereas its expansion occurs in most nanosized metal-oxides [4,5]. Since physical properties of nanoparticles are determined by their structure, an understanding of nanoscale lattice modifications is advantageous for properties tuning but is a challenging task [6–9].

In this study we have explored a size-induced relaxation of the local structure in several tungstates by extended x-ray absorption fine structure (EXAFS) spectroscopy, x-ray powder diffraction and micro-Raman spectroscopy. Our recent results on nanosized $ZnWO_4$ [10,11] have been extended to other tungstates – $CoWO_4$, $NiWO_4$ and $CuWO_4$, thus, allowing us to elucidate in more details the effect of size, temperature and transition metal type.

2. Experimental details

Nanocrystalline powders were synthesized by co-precipitation method from aqueous solutions of $Na_2WO_4 \cdot 2H_2O$ and $Co(NO_3)_2 \cdot 6H_2O$, $Ni(NO_3)_2 \cdot 6H_2O$, $CuSO_4 \cdot 5H_2O$ or $Zn(NO_3)_2 \cdot 6H_2O$ at room temperature (20 °C), pH=8 [10,11]. Microcrystalline samples were obtained by annealing of nanopowders at 800 °C for 4–8 h.

X-ray powder diffraction (XRD) patterns (Fig. 1) were recorded at 20 °C using Bragg–Brentano powder diffractometer ($\theta/2\theta$ scans) equipped with conventional copper anode (Cu $K\alpha$) tube.

Micro-Raman scattering spectra (Fig. 2) were collected in backscattering geometry at 20 °C using a confocal microscope with spectrometer Nanofinder-S (SOLAR TII, Ltd.). The measurements were performed through Nikon Plan Apo 20 × (NA=0.75) optical objective. DPSS laser (532 nm, 150 mW cw power) was used as the excitation source, and the Raman scattering spectra were dispersed by 1800 grooves/mm diffraction grating, mounted in the 520 mm focal length monochromator. The elastic laser light component was eliminated by the edge filter (Semrock LP03-532RE). The Peltier-cooled back-thinned CCD camera (ProScan HS-101H) was used as a detector.

The Fourier transform infrared (FTIR) transmission spectra (Fig. 3) were recorded at 20 °C with a Bruker Equinox 55 spectrometer using a KBr pellet technique in the range of 500–4000 cm^{-1}.

X-ray absorption measurements were performed in transmission mode at the HASYLAB/DESY C (CEMO) bending-magnet beamline [12] at the Co (7709 eV), Ni (8333 eV), Cu (8979 eV) and Zn (9659 eV) K-edges and W L_3 (10207 eV) edge. The storage ring DORIS III was operated at E=4.44 GeV and I_{max} = 140 mA. The x-ray beam intensity was measured by two ionization chambers filled with argon and krypton gases. The higher-order harmonics were effectively eliminated by detuning of the double-crystal monochromator Si(111) to 60% of the rocking curve maximum, using the beam-stabilization feedback control. The powder samples were deposited on Millipore filters and fixed by Scotch tape. The deposited powder weight was chosen to give the value of the absorption edge jump close to 1.0. Measurements were performed

* Corresponding author. Tel.: +371 67 25 16 91; fax: +371 67 13 27 78.
E-mail address: a.kuzmin@cfi.lu.lv (A. Kuzmin).
URL: http://www.cfi.lv/ (A. Kuzmin).

0038-1098/$ - see front matter © 2013 Elsevier Ltd. All rights reserved.
http://dx.doi.org/10.1016/j.ssc.2013.12.028

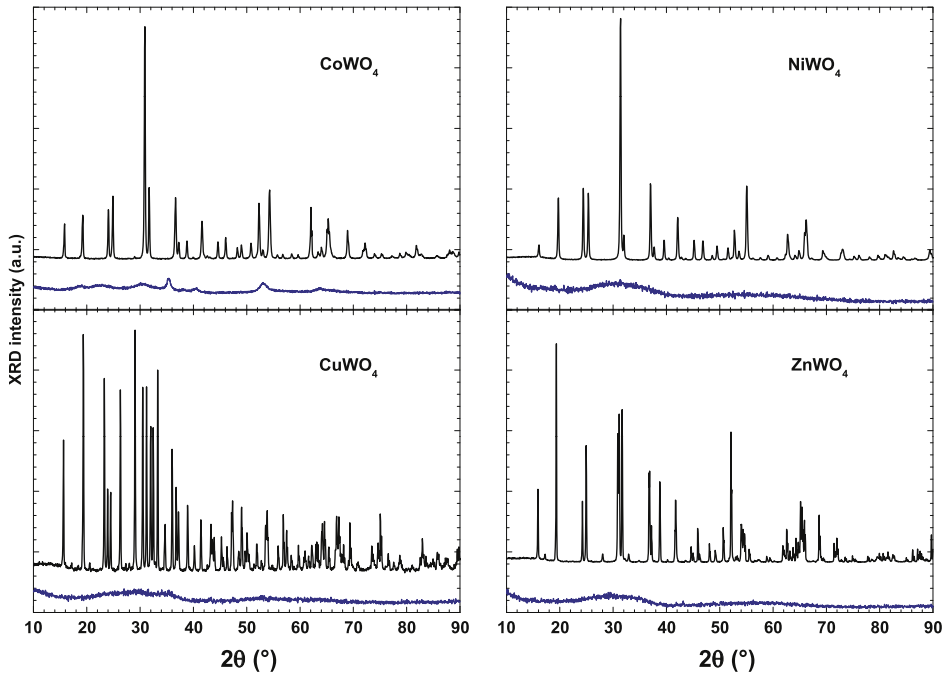

Fig. 1. (Color online). X-ray diffraction patterns of as-prepared (lower curves) and annealed at 800 °C (upper curves) $MeWO_4$ (Me=Co, Ni, Cu, Zn) powders.

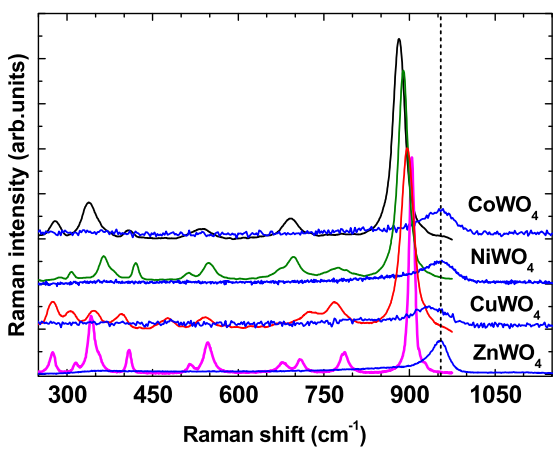

Fig. 2. (Color online). Raman scattering spectra of microcrystalline and nanosized $MeWO_4$ (Me=Co, Ni, Cu, Zn) powders. The position of the main band at 955 cm^{-1} in nanosized tungstates is indicated by dashed vertical line. Measurements were performed at 20 °C.

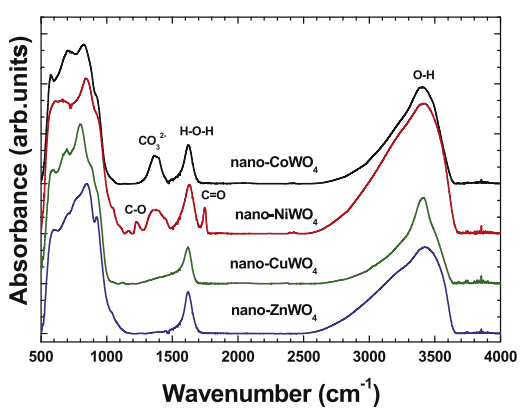

Fig. 3. (Color online). FTIR spectra of nanosized $MeWO_4$ (Me=Co, Ni, Cu, Zn) powders.

at 10 and 300 K using the Oxford Instruments liquid helium flow cryostat.

3. EXAFS data analysis

X-ray absorption spectra were analysed using the conventional procedure [13,14]. Fourier transforms (FTs) of the experimental EXAFS spectra $\chi(k)k^2$ at $T=300$ K for $CoWO_4$ and $CuWO_4$ are shown in Fig. 4. The experimental data for $NiWO_4$ and $ZnWO_4$ were reported elsewhere [15,16]. The photoelectron wavenumber is defined as $k=[(2m_e/\hbar^2)(E-E_0)]^{1/2}$, where m_e is the electron mass, $\hbar$ is the Plank's constant, and E_0 is the photoelectron energy origin. The E_0 position in the experimental signals was set at the energy point to have the best match between k-space scales of the experimental and theoretical EXAFS spectra. Note that the positions of the FT peaks in Fig. 4 are shifted from their true crystallographic values because the FTs were calculated without phase-shift corrections. In this work only the first coordination shell contributions, singled out by the back-FT procedure in the range of $\simeq 0.8$–2.2Å, were analysed.

To extract structural information, the first shell EXAFS contributions $\chi(k)k^2$ were best-fitted using a model-independent approach [17,18] allowing the reconstruction of the true radial distribution function (RDF) $G(R)$

$$\chi(k)=\int_{R_{min}}^{R_{max}}\frac{G(R)}{kR^2}F(\pi,k,R)\ \sin\left(2kR+\Phi(\pi,k,R)\right)dR, \quad (1)$$

where R is the interatomic distance, $F(\pi,k,R)$ is the scattering amplitude function, and $\Phi(\pi,k,R)$ is the phase shift function. The obtained RDFs are shown in Fig. 5.

The advantage of the method provided by Eq. (1) is that the true RDF $G(R)$ can have an arbitrary (even strongly distorted) shape [17,18]. This point is very important in the case of tungstates, especially nanocrystalline, where strong static distortion of the metal–oxygen octahedra is present [15], particularly in the case of WO_6 and CuO_6 octahedra experiencing strong Jahn–Teller distortion [19]. The significant distortion of octahedra makes the

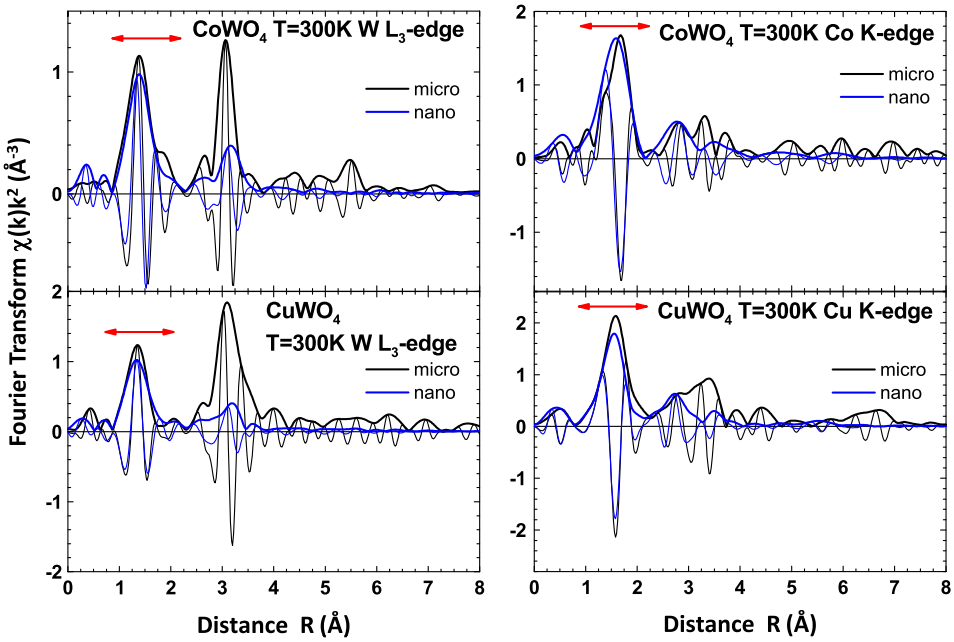

Fig. 4. (Color online). Fourier transforms (FTs) of the experimental W L_3 and Co(Cu) K edges EXAFS spectra $\chi(k)k^2$ for microcrystalline and nanoparticles Co(Cu)WO_4 at T=300 K. Both modulus and imaginary parts of FTs are shown.

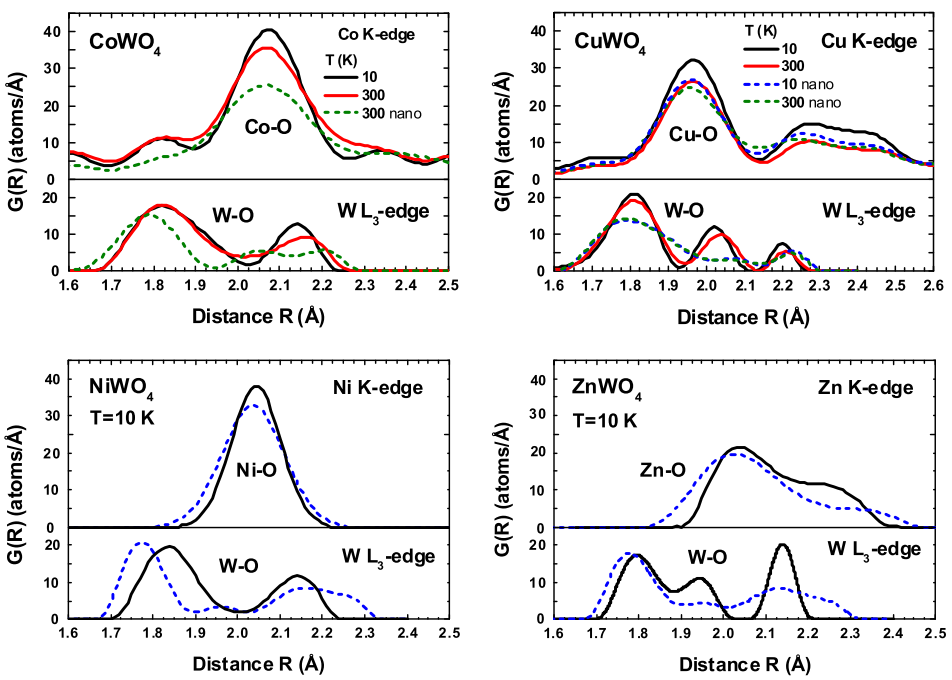

Fig. 5. (Color online). The reconstructed RDFs $G(R)$ for the first coordination shell of tungsten and transition metals in microcrystalline (solid lines) and nanosized (dashed lines) $MeWO_4$ (Me=Co, Ni, Cu, Zn). See text for details.

use of conventional EXAFS data analysis approach [13], i.e., an approximation of the RDF $G(R)$ by a set of Gaussian functions, inaccurate since such model is not able to account for an asymmetry of peaks in the RDF and is also not unique due to strong overlap between some peaks. However, the obtained RDFs can be utilized for the reconstruction of nanoparticle structure using advanced simulation techniques such as reverse Monte Carlo [20,21] or Molecular Dynamics methods [9]. This problem is beyond the scope of the present paper and will be addressed by us in future work.

Note that the scattering amplitude $F(\pi,k,R)$ and phase shift $\Phi(\pi,k,R)$ functions, used in the best-fit of the first shell EXAFS signals in Eq. (1), were independently calculated for metal–oxygen atom pairs by ab initio real-space multiple-scattering code FEFF8 [22] using the complex exchange-correlation Hedin–Lundqvist potential. The FEFF8 calculations were performed for crystalline tungstates ($CoWO_4$ [23], $NiWO_4$ [24], $CuWO_4$ [25] and $ZnWO_4$ [26,27]), constructing a cluster of 8 Å size around the absorbing metal atom. The size of the cluster allowed us to be confident in the accuracy of the calculated cluster potential and to simulate

theoretical W L_3 and Me (Me=Co, Ni Cu, Zn) K edge EXAFS spectra, required for accurate evaluation of the E_0 values. Calculations of the cluster potentials were done in the muffin-tin (MT) self-consistent-field approximation using default values of MT radii as provided within the FEFF8 code [22].

4. Results

The XRD patterns for all as-prepared powders of tungstates have strongly broadened Bragg peaks (Fig. 1). Since the Raman scattering spectra of as-prepared powders are close and also strongly broadened (Fig. 2), and their EXAFS signals do not contain significant outer shell (beyond ~4 Å) contributions (Fig. 4), we concluded that our samples are mainly composed of very fine (less than about 2 nm) nanocrystallites [10,11]. However, some larger nanocrystallites are present in $CoWO_4$ sample and are responsible for few small Bragg peaks in Fig. 1. Their relative amount is nevertheless small, so that they do not produce any observable contribution into Raman scattering and EXAFS spectra.

Note that the tungstate powders become microcrystalline upon annealing in air at 800 °C [10], showing XRD patterns corresponding to respective wolframite phases with monoclinic ($CoWO_4$ [23], $NiWO_4$ [24], $ZnWO_4$ [26,27]) or triclinic ($CuWO_4$ [25]) symmetry.

The Raman scattering spectra of microcrystalline tungstates are shown in Fig. 2. Since they have two formula units ($Z=2$) per primitive cell, the group theory analysis predicts 36 lattice modes, of which 18 even vibrations are Raman active [19,28–30]. Only twelve of them can be observed in the frequency range reported in Fig. 2. The position of the most intense band, located at 882–905 cm^{-1} and corresponding to the stretching W–O vibration, shifts systematically to higher frequencies upon transition from $CoWO_4$ to $ZnWO_4$. The Raman scattering spectra of nanoparticles differ significantly from that in microcrystalline powders. They are dominated by one broad band, located at ~955 cm^{-1}. One should note that care should be taken when measuring the Raman scattering from tungstate nanoparticles, since they can be easily crystallized under excessive laser irradiation.

FTIR spectra of nanocrystalline tungstates are shown in Fig. 3. The group of peaks in the range of 500–1000 cm^{-1} is due to the odd bending and stretching vibrations of tungstate lattice [31,30,19]. A strong broad IR band located at ~3400 cm^{-1} is attributed to the O–H stretching modes due to the presence of hydroxyl as well as adsorbed water, and a band at ~1620 cm^{-1} is due to the H–O–H bending vibrations of water molecules [32,33]. Besides the bands at ~1750 cm^{-1} and ~1225 cm^{-1}, observed only in nano-$NiWO_4$, can be ascribed to the C=O and C–O stretching modes [34,35], and the band at ~1370 cm^{-1} indicates the existence of CO_3^{2-} ions [35] in nano-$CoWO_4$ and nano-$NiWO_4$.

Fourier transforms of the experimental W L_3 and Co(Cu) K edges EXAFS spectra $\chi(k)k^2$ are shown in Fig. 4. The amplitude of all peaks, especially beyond the first one, is strongly reduced in nanopowders, as expected. The effect is more pronounced at the W L_3-edge, indicating stronger relaxation of tungsten environment. The RDFs for the first coordination shell around metal atoms were extracted, as described in Section 3, from the first peak in FTs and are shown in Fig. 5 for all microcrystalline (solid lines) and nanosized (dashed lines) tungstates. They correspond to the distribution of oxygen atoms within metal–oxygen octahedra. A comparison of the RDFs obtained at 10 and 300 K in $CuWO_4$ suggests that the effect of thermal disorder leads to some peak broadening and is relatively small, in particular, in nanopowders where static relaxation dominates.

In microcrystalline $CoWO_4$ [23] and $NiWO_4$ [24] the six oxygen atoms of slightly distorted Co(Ni)O_6 octahedra contribute into one broad peak, centered at ~2.08 Å in the RDF $G_{Co-O}(R)$ and at ~2.05 Å in the RDF $G_{Ni-O}(R)$. The WO_6 octahedra in both tungstates are strongly distorted: the six oxygens are divided into two groups of four (at ~1.83 Å) and two (at ~2.15 Å) atoms.

In microcrystalline $CuWO_4$ [25] the RDF $G_{Cu-O}(R)$ is split into two peaks, composed of four and two oxygen atoms. At the same time, the distortion of WO_6 octahedra is the strongest one among all four tungstates: six oxygen atoms are divided into 3 groups of three (at ~1.81 Å), two (at ~2.02 Å) and one (at ~2.20 Å) atoms.

The distortion of metal–oxygen octahedra in microcrystalline $ZnWO_4$ [26,27] is stronger than in $CoWO_4$ and $NiWO_4$, but weaker than in $CuWO_4$. The oxygen atoms in both ZnO_6 and WO_6 octahedra are divided into three groups of two oxygen atoms each. The group of nearest four oxygens is responsible for a single peak at ~2.02 Å in the RDF $G_{Zn-O}(R)$, whereas remaining two oxygens give rise to the peak at ~2.25 Å. In the case of the RDF $G_{W-O}(R)$, the three groups of oxygen atoms are well resolved and contribute into the three peaks at ~1.80 Å, ~1.95 Å and ~2.14 Å.

In nanosized tungstates, the RDFs $G_{Me-O}(R)$ are more broadened. Besides, the distortion of ZnO_6 octahedra becomes stronger in nano-$ZnWO_4$, leading to further separation of nearest four and distant two oxygen atoms. The modification of the RDFs $G_{W-O}(R)$ is more dramatic. The distortion of WO_6 octahedra increases in all tungstates in such a way that the nearest four oxygen atoms move slightly closer, whereas the distant two oxygens move away. This effect is most evident in the RDFs $G_{W-O}(R)$ for nanosized $NiWO_4$, $CoWO_4$ and $ZnWO_4$.

5. Discussion

The absence of Bragg peaks in XRD patterns of nanoparticles (Fig. 1) suggests that the size of crystallites in as-prepared powders is below 2 nm. Taking into account nanoparticles stoichiometry, the size of metal–oxygen octahedra (~4 Å) and their connectivity in crystalline tungstates, one can conclude that nanoparticles are built up of just a few metal–oxygen octahedra.

Chemical bonding in microcrystalline tungstates can be successfully probed by Raman spectroscopy, providing an access to the half of vibrational modes (Fig. 2). An increase of the stretching W–O frequency from 882 cm^{-1} in $CoWO_4$ to 905 cm^{-1} in $ZnWO_4$ indicates some strengthening of tungsten–oxygen bonds [36], which compete with the Me–O bonding. Note that the corresponding W–O bond lengths are almost equal (~1.79 Å) in the four tungstates [23–27].

Nanosized tungstates are much weaker Raman scatterers (Fig. 2): the only visible broad band at ~955 cm^{-1} was attributed previously to the double tungsten–oxygen W=O bonds at the nanoparticle surface [10]. The band has a single-peak shape in $CoWO_4$, $NiWO_4$ and $ZnWO_4$, but has more complex structure in $CuWO_4$, suggesting the presence of slightly inequivalent non-bridging W=O bonds. A well known correlation [36] between the force constant (or stretching frequency) and the length of the W–O bond suggests the W=O bond length of about 1.7 Å.

In fact, the existence of short tungsten–oxygen bonds in nanopowders is clearly visible in the RDFs $G_{W-O}(R)$ (Fig. 5). In general, the WO_6 octahedra distortion originates from strong electron–lattice coupling, which leads to the second-order Jahn–Teller (SOJT) effect due to a covalent interaction of empty 5*d* orbitals in W^{6+} ions with filled 2*p* orbitals in the oxygen atoms [37]. An additional contribution into the WO_6 octahedron deformation comes from competing interaction of oxygens with the 3*d* transition metal ions. It manifests most strongly in $CuWO_4$, where the axial distortion of CuO_6 octahedra is stabilized by the first-order Jahn–Teller (FOJT) effect caused by the $3d^9$ electron

configuration of Cu^{2+} ions [19,38–40]. As a result, the RDFs $G_{Cu-O}(R)$ have close shape in both microcrystalline and nanosized powders, and the difference between the RDFs $G_{W-O}(R)$ is caused mainly by peak broadening.

In $CoWO_4$, $NiWO_4$ and $ZnWO_4$, the bonding between 3*d* and oxygen ions is less rigid, so that their local environment is able to relax in nanopowders, giving more freedom to tungsten ions to adapt themselves. Therefore, tungsten ions are able to attract four nearest oxygens, thus enhancing the distortion of WO_6 octahedra. The remaining two oxygen atoms are weakly bonded to tungsten and are responsible for the distant peak in the RDF at $\sim$2.1–2.3 Å (Fig. 5). Such values of the tungsten–oxygen bonds are typical for W–OH_2 bonding in hydrates $WO_3 \cdot nH_2O$ [36,32] and for W–OH bonds at the tungsten oxide surface [41]. Note that in hydrates the W–OH_2 bonds are located opposite to the short terminal W=O bonds [36], discussed above. The presence of OH groups or H_2O molecules in our nanocrystalline powders, evidenced by FTIR spectra in Fig. 3, follows from the synthesis procedure (see Section 2) and is required to maintain nanoparticle electroneutrality.

6. Conclusions

In this study we have performed an investigation of the local atomic structure of nanosized and microcrystalline tungstates $MeWO_4$ (Me=Co, Ni, Cu, Zn), synthesized by co-precipitation technique. We have employed x-ray absorption spectroscopy at the W L_3-edge and Co/Ni/Cu/Zn K-edges as the main tool. A set of complementary techniques as x-ray diffraction, Raman and Fourier transform infrared spectroscopies have been also used.

The analysis of the EXAFS spectra by the regularization-like method has allowed us to reliably determine a distortion of WO_6 and MeO_6 octahedra in microcrystalline and nanosized tungstates. The distortion is caused by the electron–lattice coupling, which depends on the electronic structure of Me^{2+} and W^{6+} ions. Additional structure relaxation in nanosized tungstates induces further deformation of the octahedra and a formation of the double tungsten–oxygen bonds, being responsible for the broad band at $\sim$955 cm^{-1} in Raman scattering spectra.

The obtained information on the structure relaxation in nanosized tungstates is relevant for understanding and tuning of their functional properties [15,42,43].

Acknowledgments

This study was supported by European Social Fund ("Support for Doctoral Studies at University of Latvia) and Latvian Science Council Grant no. 187/2012. The EXAFS experiments at HASYLAB/DESY were supported by the EC FP7 under Grant Agreement no. 226716.

References

[1] C.Q. Sun, Prog. Solid State Chem. 35 (2007) 1.
[2] P.A. Montano, G.K. Shenoy, E.E. Alp, W. Schulze, J. Urban, Phys. Rev. Lett. 56 (1986) 2076.
[3] R. Lamber, S. Wetjen, N.I. Jaeger, Phys. Rev. B 51 (1995) 10968.
[4] M. Fukuhara, Phys. Lett. A. 313 (2003) 427.
[5] G. Li, J. Boerio-Goates, B.F. Woodfield, L. Li, Appl. Phys. Lett. 85 (2004) 2059.
[6] A. Witkowska, A. Di Cicco, E. Principi, Phys. Rev. B 76 (2007) 104110.
[7] A.I. Frenkel, A. Yevick, C. Cooper, R. Vasic, Annu. Rev. Anal. Chem. 4 (2011) 23.
[8] G. Greco, A. Witkowska, E. Principi, M. Minicucci, A. Di Cicco, Phys. Rev. B 83 (2011) 134103.
[9] A. Anspoks, A. Kalinko, R. Kalendarev, A. Kuzmin, Phys. Rev. B 86 (2012) 174114.
[10] A. Kalinko, A. Kuzmin, J. Lumin. 129 (2009) 1144.
[11] A. Kalinko, A. Kotlov, A. Kuzmin, V. Pankratov, A.I. Popov, L. Shirmane, Cent. Eur. J. Phys. 9 (2011) 432.
[12] K. Rickers, W. Drube, H. Schulte-Schrepping, E. Welter, U. Bruggmann, M. Herrmann, J. Heuer, H. Schulz-Ritter, in: AIP Conference Proceedings, vol. 882, 2007. p. 905.
[13] V.L. Aksenov, A.Y. Kuzmin, J. Purans, S.I. Tyutyunnikov, Phys. Part. Nucl. 32 (2001) 675.
[14] A. Kuzmin, Physica B 208–209 (1995) 175.
[15] A. Kalinko, A. Kuzmin, J. Non-Cryst. Solids 357 (2011) 2595.
[16] A. Kuzmin, V. Pankratov, A. Kalinko, A. Kotlov, L. Shirmane, A.I. Popov, J. Phys. Conf. Ser., 2014 (in press).
[17] A. Kuzmin, J. Phys. IV (Fr.) 7 (1997) C2–C213.
[18] A. Kuzmin, J. Purans, J. Phys.: Condens. Matter 12 (2000) 1959.
[19] A. Kuzmin, A. Kalinko, R. Evarestov, Acta Mater. 61 (2013) 371.
[20] N. Bedford, C. Dablemont, G. Viau, P. Chupas, V. Petkov, J. Phys. Chem. C 111 (2007) 18214.
[21] J. Timoshenko, A. Kuzmin, J. Purans, Comput. Phys. Commun. 183 (2012) 1237.
[22] A.L. Ankudinov, B. Ravel, J.J. Rehr, S.D. Conradson, Phys. Rev. B 58 (1998) 7565.
[23] J.B. Forsyth, C. Wilkinson, J. Phys.: Condens. Matter 6 (1994) 3073.
[24] H. Weitzel, Z. Kristallogr. 144 (1976) 238.
[25] J.B. Forsyth, C. Wilkinson, A.I. Zvyagin, J. Phys.: Condens. Matter 3 (1991) 8433.
[26] P.F. Schofield, K.S. Knight, G. Cressey, J. Mater. Sci. A 31 (1996) 2873.
[27] D.M. Trots, A. Senyshyn, L. Vasylechko, R. Niewa, T. Vad, V.B. Mikhailik, H. Kraus, J. Phys.: Condens. Matter 21 (2009) 325402.
[28] Y. Liu, H. Wang, G. Chen, Y.D. Zhou, B.Y. Gu, B.Q. Hu, J. Appl. Phys. 64 (1988) 4651.
[29] H. Wang, F.D. Medina, Y.D. Zhou, Q.N. Zhang, Phys. Rev. B 45 (1992) 10356.
[30] A. Kuzmin, A. Kalinko, R.A. Evarestov, Cent. Eur. J. Phys. 9 (2011) 502.
[31] R.A. Evarestov, A. Kalinko, A. Kuzmin, M. Losev, J. Purans, Integr. Ferroelectr. 108 (2009) 1.
[32] M. Gotić, M. Ivanda, S. Popović, S. Musić, Mater. Sci. Eng. B – Adv. 77 (2000) 193.
[33] G. Huang, Y. Zhu, Mater. Sci. Eng. B 139 (2007) 201.
[34] J.H. Ryu, C.S. Lim, K.H. Auh, Mater. Lett. 57 (2003) 1550.
[35] J. Li, R. Yan, B. Xiao, D.T. Liang, D.H. Lee, Energy Fuels 22 (2008) 16.
[36] M.F. Daniel, B. Desbat, J.C. Lassegues, B. Gerand, M. Figlarz, J. Solid State Chem. 67 (1987) 235.
[37] M. Kunz, I. Brown, J. Solid State Chem. 115 (1995) 395.
[38] J. Ruiz-Fuertes, D. Errandonea, R. Lacomba-Perales, A. Segura, J. González, F. Rodríguez, F.J. Manjón, S. Ray, P. Rodríguez-Hernández, A. Muñoz, Z. Zhu, C.Y. Tu, Phys. Rev. B 81 (2010) 224115.
[39] J. Ruiz-Fuertes, A. Friedrich, J. Pellicer-Porres, D. Errandonea, A. Segura, W. Morgenroth, E. Haussühl, C.-Y. Tu, A. Polian, Chem. Mater. 23 (2011) 4220.
[40] J. Ruiz-Fuertes, A. Segura, F. Rodríguez, D. Errandonea, M.N. Sanz-Ortiz, Phys. Rev. Lett. 108 (2012) 166402.
[41] A. Kuzmin, J. Purans, E. Cazzanelli, C. Vinegoni, G. Mariotto, J. Appl. Phys. 84 (1998) 5515.
[42] S.M. Montemayor, A.F. Fuentes, Ceram. Int. 30 (2004) 393.
[43] P. Schmitt, N. Brem, S. Schunk, C. Feldmann, Adv. Funct. Mater. 21 (2011) 3037.